

# Visualizing and Quantifying Wettability Alteration by Silica Nanofluids

Shidong Li,<sup>\*,†</sup> Anqi Sng,<sup>‡</sup> Dan Daniel,<sup>\*,‡</sup> Hon Chung Lau,<sup>¶</sup> Ole Torsæter,<sup>§,||</sup> and  
Ludger P. Stubbs<sup>†</sup>

<sup>†</sup>*Institute of Chemical and Engineering Sciences (ICES), Agency for Science, Technology  
and Research (A\*STAR), 1, Pesek Road, Jurong Island, Singapore, 627833*

<sup>‡</sup>*Institute of Materials Research and Engineering, Agency for Science, Technology and  
Research (A\*STAR), 2 Fusionopolis Way, Innovis, Singapore 138634*

<sup>¶</sup>*Department of Civil and Environmental Engineering, National University of Singapore, 1  
Engineering Drive 2, Singapore, 117576*

<sup>§</sup>*PoreLab, Norwegian Center of Excellence, S. P. Andersens vei 15b, Trondheim, Norway,  
7031*

<sup>||</sup>*Department of Geoscience and Petroleum, Norwegian University of Science and  
Technology (NTNU), S.P. Andersens veg 15a, Trondheim, Norway, 7031*

E-mail: li\_shidong@ices.a-star.edu.sg/lisd\_pe@hotmail.com; daniel@imre.a-star.edu.sg

## Abstract

1  
2 An aqueous suspension of silica nanoparticles or nanofluid can alter the wettability  
3 of surfaces, specifically by making them hydrophilic and oil-repellent under water. Wet-  
4 tability alteration by nanofluids have important technological applications, including  
5 for enhanced oil recovery and heat transfer processes. A common way to characterize  
6 the wettability alteration is by measuring the contact angles of an oil droplet with and  
7 without nanoparticles. While easy to perform, contact angle measurements do not fully

8 capture the wettability changes to the surface. Here, we employed several complemen-  
9 tary techniques, such as cryo-scanning electron microscopy, confocal fluorescence and  
10 reflection interference contrast microscopy and droplet probe atomic force Microscopy  
11 (AFM), to visualize and quantify the wettability alterations by fumed silica nanoparti-  
12 cles. We found that nanoparticles adsorbed onto glass surfaces to form a porous layer  
13 with hierarchical micro- and nano-structures. The porous layer is able to trap a thin  
14 water film, which reduces contact between the oil droplet and the solid substrate. As  
15 a result, even a small addition of nanoparticles (0.1 wt%) lowers the adhesion force  
16 for a 20- $\mu$ m-sized oil droplet by more than 400 times from  $210\pm 10$  nN to  $0.5\pm 0.3$  nN  
17 as measured using droplet probe AFM. Finally, we show that silica nanofluids can  
18 improve oil recovery rates by 8% in a micromodel with glass channels that resemble a  
19 physical rock network.

## 20 **Keywords**

21 Nanofluids; Enhanced Oil Recovery; Reflection Interference Contrast Microscopy; Droplet  
22 Probe Atomic Force Microscopy; Wettability Alteration

## 23 **Introduction**

24 Suspensions of nanoparticles or nanofluids have many important technological applications,  
25 including for enhanced heat transfer and oil recovery processes.<sup>1,2</sup> The wetting properties of  
26 surfaces are altered when nanoparticles adsorb onto the surface;<sup>3</sup> for example, with silica and  
27 other metal oxide nanoparticles, the surface becomes more water-wettable or hydrophilic.  
28 This greatly improves the heat transfer rates during boiling by preventing air bubbles (which  
29 conduct heat poorly) from accumulating on the surface.<sup>4</sup> In enhanced oil recovery (EOR)  
30 processes, nanoparticles allow oil trapped in the porous network to be more easily extracted  
31 by water injection.<sup>5-7</sup>

32 The wettability of oil reservoirs plays a critical role in EOR. It can affect the oil-water  
33 relative permeability, capillary pressure and therefore the residual oil distribution. Suitably  
34 altering reservoir's wettability, such as using nanofluids, can increase oil recovery. For ex-  
35 ample, nanoparticles can change the wettability of a carbonate reservoirs from hydrophobic  
36 to hydrophilic, improving oil recovery.<sup>8,9</sup> The wettability alteration mechanisms of nanofluid  
37 have been investigated previously. They include structural disjoining pressure,<sup>8</sup> increase  
38 of surface roughness, reduction of surface free energy,<sup>10</sup> electrostatic repulsion promotion,  
39 decline of non-electrostatic adhesion force and structural interaction force,<sup>11</sup> nanoparticle  
40 layering near the solid substrate,<sup>12</sup> and partial release of stearate from the calcite surface  
41 and replacement by silica nanoparticles.<sup>9</sup>

42 One method to quantify surface wettability alteration is by measuring the contact an-  
43 gles  $\theta$  made by air bubbles (for boiling) and oil droplets (for oil recovery processes) under  
44 water. For example, adding 0.5 wt% fumed silica nanoparticles increases  $\theta$  from  $141^\circ$  to  
45 nearly  $180^\circ$  for millimetre-sized crude oil droplet (Fig. 1); the glass substrate has become  
46 more hydrophilic. For large oil droplets on flat surfaces, the contact angles can be deduced  
47 optically from high-resolution sideview images of the droplets as shown in Figure 1. For oil  
48 trapped inside a porous network, the contact angles at the pore-scale can be measured from  
49 X-ray micro-computed tomography (micro-CT) images,<sup>13,14</sup> which makes this technique par-  
50 ticularly suited to understand oil-recovery processes. While powerful and easy to perform,  
51 contact angle measurements suffer from several disadvantages.<sup>15,16</sup> Contact angle measure-  
52 ments are inaccurate for large values close to  $180^\circ$  (including in Fig. 1b); a small error in  
53 the positioning of the droplet base (as small as a single pixel) translates to a large error  
54 in the contact angle value (of more than  $10^\circ$ ).<sup>17,18</sup> More importantly, the sideview droplet  
55 images in contact angle measurements do not allow us to visualize the three-phase contact  
56 line which is better captured from the bottom of the droplet.

57 Previously, AFM with a sharp solid tip has been used to probe properties of rock surfaces  
58 relevant to the oil industry, including their topography, mechanical and chemical proper-

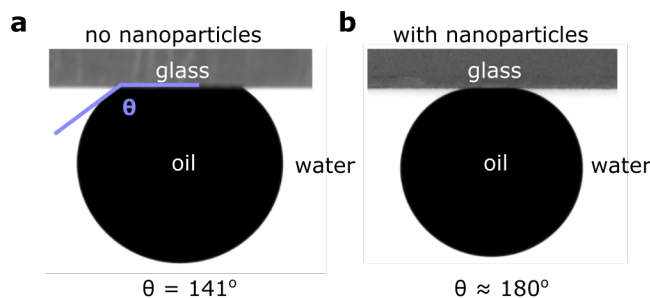


Figure 1: Underwater contact angle of crude oil droplets in the absence and presence of nanoparticles.

ties.<sup>19,20</sup> The AFM tip can also be functionalized with different organic groups (chemical force microscopy) to mimic the interactions between different oil components and the solid substrate.<sup>11,21–23</sup> Intermolecular forces and the adhesion between the chemically-modified tips and substrate can be measured with piconewton resolutions, and wettability alterations can be resolved spatially with submicron resolutions using this technique. Chemical force microscopy with its solid tip cannot however fully capture the interactions of a liquid droplet with a solid substrate.

Here, we propose two techniques, namely reflection interference contrast microscopy (RICM) and droplet probe AFM, that are highly complementary to contact angle measurement and chemical force microscopy, respectively. RICM allows us to observe the droplet's base as opposed to sideview images in contact angle measurements, while droplet probe AFM allows us to measure the interaction forces of a microdroplet (as opposed to a solid tip) with the substrate.

We used the two techniques to visualize and quantify wettability alterations by fumed silica nanoparticles, chosen for their low cost and wide availability. Our previous studies also demonstrated the effectiveness of fumed silica in EOR: the injection of 0.05 wt% fumed silica suspension improves oil recovery from a core plug by 6%.<sup>24</sup> First, we used cryo-scanning electron microscopy (cryo-SEM) and atomic force microscopy (AFM) to visualize and measured the thickness of adsorbed nanoparticles on a glass surface. We found that the nanoparticles form a porous layer with hierarchical micro- and nano-structures that stabilizes a thin water

79 film beneath the oil droplet, which we confirmed using a combination of confocal fluores-  
80 cence and RICM.<sup>25,26</sup> With RICM, we show that the oil droplet is in contact only with the  
81 topmost tips of the porous layer (Cassie-Baxter state);<sup>27</sup> as a result, the oil droplet has a  
82 high underwater contact angle  $\theta$  close to  $180^\circ$  with minimal adhesion, reminiscent of the un-  
83 derwater superoleophobicity exhibited by fish scales and artificial bioinspired surfaces.<sup>28</sup> We  
84 also use droplet probe AFM to directly measure the interaction forces (with a resolution of  
85 less than 1 nN) between an oil microdroplet and a glass surface under different nanoparticle  
86 concentrations.<sup>29-31</sup> We show that fumed silica can reduce the adhesion force and the energy  
87 required to remove oil microdroplets by more than 400 and 7000 times, respectively. We also  
88 observed force jumps in the force curves corresponding to pinning and depinning dynamics  
89 of the contact line.

90 When combined together, the techniques described in this paper are able to probe changes  
91 in the surface structural and wetting properties by nanofluids in unprecedented details,  
92 and highly complement previously described techniques. The techniques presented allow  
93 us to better understand an important aspect of how wettability alteration is achieved by  
94 nanofluids: the adsorbed nanoparticles are able to stabilize a thin water film beneath the  
95 oil droplet. With RICM, we are able to visualize this water film and the pinning points  
96 directly, while droplet probe AFM allows us to measure the adhesion due to the pinning  
97 points, including the dynamics of contact line pinning-depinning. Finally, we demonstrate  
98 the effect of wettability alteration on the effectiveness of oil recovery in a micromodel with  
99 glass channels that resemble a physical rock network and observed an improvement in oil  
100 recovery rate of 8%.

## 101 **Results and discussion**

### 102 **Structure of adsorbed nanoparticles**

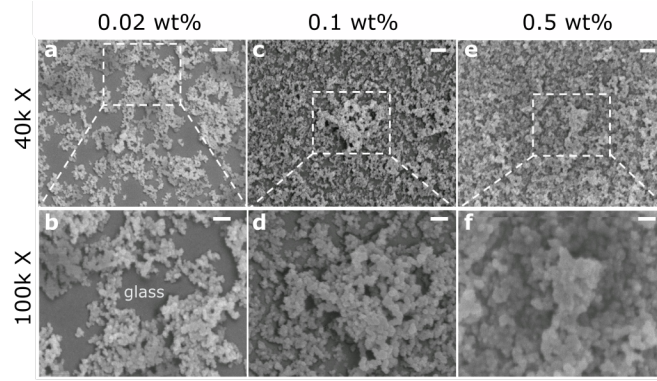


Figure 2: Cryo-SEM of adsorbed nanoparticles at different particle concentrations 0.02–0.5 wt% and under 40,000 $\times$  and 100,000 $\times$  magnifications. Scale bars are 200 nm for (a, c, e) and 100 nm for (b, d, f).

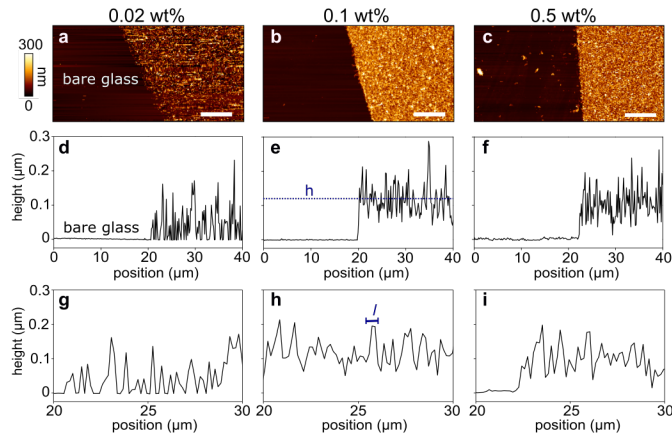


Figure 3: (a–c) The thickness and the roughness of the nanoparticle layer can be determined using atomic force microscopy for different particle concentrations. Scale bars are 5  $\mu\text{m}$ . (d–f) Cross-sections of the nanoparticle layer for the different particle concentrations and (g–i) zoomed-in views of the cross-sections.

103 We first used cryo-SEM to visualize the adsorbed nanoparticles (average primary particle  
 104 size  $s$  is 7 nm) on a glass surface, after it is immersed in brine solution (3 wt% NaCl in water)  
 105 containing different particle concentrations from 0.02 to 0.5 wt% for an hour. 3 wt% NaCl  
 106 is used because this is close to the salt content found in seawater which is widely used in  
 107 EOR applications. In DI water, both glass and silica surface are negatively charged, and  
 108 in the absence of any salt, the electric double layer forces are sufficiently repulsive to keep  
 109 the nanoparticles in solution.<sup>32</sup> The addition of NaCl salt can however screen the double  
 110 layer forces and promotes the aggregation and adsorption of nanoparticles; as a result, the

111 nanoparticles form porous structures with hierarchical micro- and nano-sized features on  
112 glass surfaces.<sup>33</sup> At the lowest particle concentration of 0.02 wt%, the surface is only partially  
113 covered with nanoparticles and bare glass is visible on the cryo-SEM image (Fig. 2a, b); in  
114 contrast, there is full coverage of nanoparticles above 0.1 wt% particle concentration (Fig. 2c–  
115 f). Note that before imaging in cryo-SEM, the surface is flash frozen using liquid nitrogen  
116 while still wet to preserve the original structures of the nanoparticle aggregates.

117 The thickness of the nanoparticle layer  $h$  can be determined by performing AFM at the  
118 boundary between the adsorbed layer and bare glass (Figs. 3a–c, See Materials and Methods  
119 for experimental details). Experimentally, we found that  $h = 47 \pm 46, 120 \pm 35, 108 \pm 40$  nm  
120 for 0.02, 0.1 and 0.5 wt% particle concentrations, respectively (Figs. 3d–f). The reported  
121 errors in  $h$  are the arithmetic mean roughness  $R_a$ .

122 Since the nanoparticle aggregates have a typical lateral dimension  $l$  of about 1 micron  
123 (Figs. 3g–i), we can estimate the number of particles in each aggregate  $N \sim hl^2/s^3 \approx 10^5$ .  
124 Note that there may be aggregates with features larger than reported here but not be picked  
125 up because of the inherently small scan range of the AFM technique (typically less than 0.1  
126 mm).

127 As will be discussed in the next sections, the presence of this nanoparticle layer with  
128 hierarchical micro- and nano-sized features have important consequences for the surface  
129 wetting properties.

## 130 **Water film stabilized by nanofluid**

131 In the absence of nanoparticles, a millimetric-sized oil droplet is in contact with the under-  
132 lying glass substrate when submerged under water, as shown in the schematic of Fig. 4a.  
133 The micrograph in Fig. 4b, taken using confocal reflection interference contrast microscopy  
134 (RICM),<sup>25,26</sup> shows the edge of the droplet's base at the three-phase contact line. In confocal  
135 RICM, the surface is raster scanned with a focused beam of monochromatic light (wavelength  
136  $\gamma=561$  nm) and the intensity of the reflected signal  $R$  increases with increasing refractive

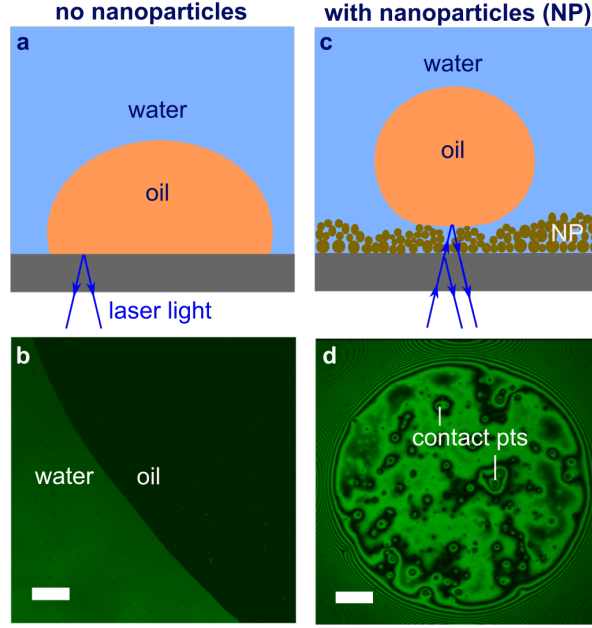


Figure 4: (a, b) Schematic and micrograph showing the oil droplet in contact with the glass substrate with no nanoparticles. Scale bar is  $100\mu\text{m}$ . (c, d) The nanoparticles are able to stabilize a thin water film beneath the oil droplet and the droplet is in contact only with the topmost tips of the nanoparticle aggregates. Scale bar is  $100\mu\text{m}$ .

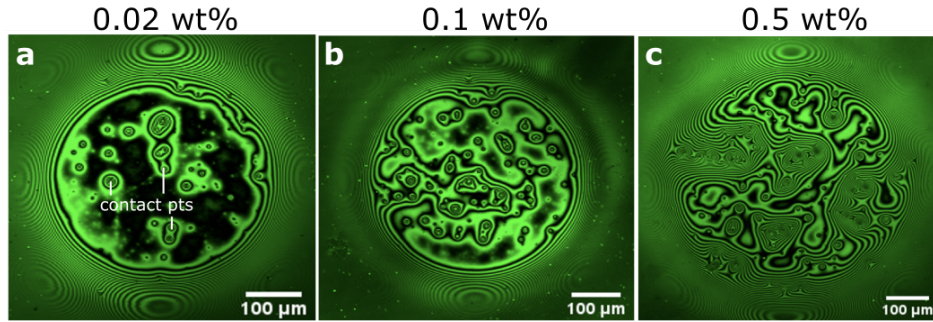


Figure 5: Droplet's base as observed using RICM for different particle concentrations. Scale bars are  $100\mu\text{m}$ .

137 index contrast  $\Delta n$ :  $R \propto \Delta n^2$ .<sup>34</sup> Hence, the droplet's base appears much darker than the  
 138 surrounding, because of the smaller  $\Delta n$  between glass and the silicone oil chosen ( $n_{\text{glass}} =$   
 139  $1.52$ ,  $n_{\text{oil}} = 1.51$ ,  $\Delta n = 0.01$ ) compared to  $\Delta n$  between glass and water ( $n_{\text{water}} = 1.33$ ,  $\Delta n$   
 140  $= 0.19$ ). Details of the technique can be found in our previous publication.<sup>26</sup>

141 In contrast, there is no direct contact between the same silicone oil droplet ( $\sim 4\text{ mm}$   
 142 diameter) and the underlying substrate with the addition of  $0.1\text{ wt}\%$  nanoparticles (Fig. 4c).

143 The micrograph in Fig. 4d shows the droplet’s base ( $\sim 0.5$  mm in size) which appear as a  
144 circular patch; the adsorbed particle layer stabilizes a thin water film beneath the droplet,  
145 which result in bright and dark fringes as lights reflected off the glass-water and water-oil  
146 interfaces interfere constructively or destructively depending on the local film thickness.  
147 The difference in water film thickness  $\Delta h_{\text{water}}$  between adjacent bright and dark fringes  
148 is  $\sim \lambda/4n_{\text{water}} \approx 200$  nm; at 0.1 wt% particle concentration, the variation in water film  
149 thickness ( $\sim 200$  nm) is small compared to the size of the droplet’s base ( $\sim 0.5$  mm).

150 The water film can be stabilized with as little as 0.02 wt% nanoparticle concentration  
151 (Fig. 5a), even though the nanoparticle surface coverage at this concentration is only partial  
152 (See Fig. 2). As we increase the particle concentration to 0.5 wt% (Fig. 5c), the water film  
153 thickness under the droplet is no longer uniform, as the droplet’s base conform to the shape  
154 of the larger aggregates. RICM therefore allows us to observe the droplet’s base directly,  
155 including the three-phase contact line and pinning points, not easily visualized from the  
156 sideview images in contact angle measurements. Here, we show that the oil droplet is in  
157 contact only with the topmost tips of the aggregates, i.e. Cassie-Baxter state, which appear  
158 as dots surrounded by interference rings on the micrograph (Fig. 4d and Fig. 5a). As will  
159 be shown in the next section, each of these contacts will act discrete pinning points which  
160 can be detected and quantified using droplet probe AFM. Note that the RICM images were  
161 taken 15 minutes after the oil droplet was deposited and no more changes to the droplet’s  
162 base and contact line were observed.

## 163 **Reduction in oil droplet adhesion**

164 We attached a silicone oil droplet (diameter  $2R = 20$   $\mu\text{m}$ ) onto a tipless cantilever probe  
165 with a flexural spring constant of  $k_z = 0.2$  N m $^{-1}$  (Fig. 6a, b). The force acting on the  
166 droplet  $F$  as it approaches and retracts from the surface at a controlled speed  $U = 2$   $\mu\text{m s}^{-1}$   
167 is obtained from the cantilever deflection  $\delta_z$ , since  $F = k_z \delta_z$ .<sup>35</sup> We chose a relatively low  $U$  to  
168 minimize viscous forces and hence observe the dynamics of contact line pinning-depinning.

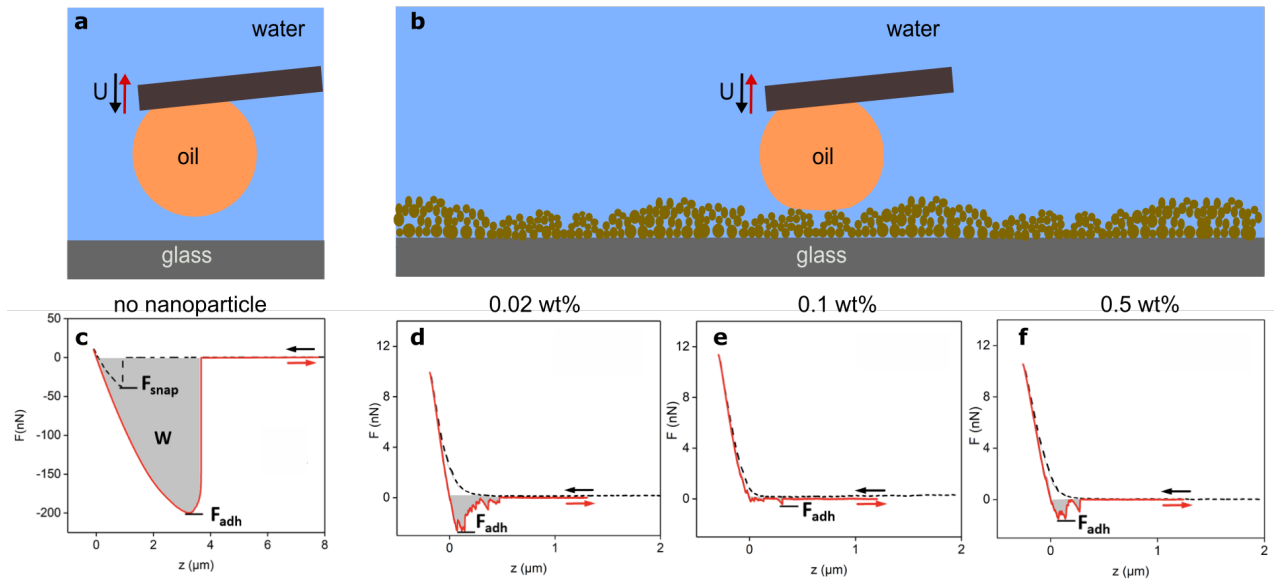


Figure 6: Droplet probe AFM can be used to quantify the interaction forces between an oil microdroplet and the surface. (a, b) Schematic showing droplet probe AFM for surfaces without and with nanoparticles. (c) Adhesion force measurement curve for the case with no nanoparticles. (d–f) Adhesion force measurement curves for the surface treated with 0.02–0.5 wt% nanoparticles.

169 Figure 6c shows the force spectroscopy measurements for a glass surface with no nanopar-  
 170 ticles, with the approach and retract curves indicated by black dashed and red solid lines,  
 171 respectively. When the droplet was far from the surface, the AFM did not detect any force,  
 172 i.e.  $F = 0$  (Fig. 6c, dashed black line); however, upon contact, there was a sudden attractive  
 173 snap-in force  $F_{\text{snap}} = 39$  nN. We continued to press onto the microdroplet to the maximum  
 174 loading force of 10 nN, before retracting (Fig. 6c, solid red line). For the droplet to be com-  
 175 pletely detached from the surface, there is a maximum adhesion force that must be overcome  
 176  $F_{\text{adh}} = 210$  nN. By integrating under the retract curve, we can also obtain the amount of  
 177 work required to remove the droplet,  $W = 0.6$  pJ, which is a significant fraction of the total  
 178 surface energy of the droplet  $4\pi R^2\gamma \approx 5$  pJ where  $\gamma$  is the surface tension, reflecting the fact  
 179 that the oil droplet strongly adheres to glass in the absence of nanoparticles.

180 The results of force spectroscopy measurements are qualitatively different with the addi-  
 181 tion of nanoparticles (Fig. 6d–f and Table 1).  $F_{\text{snap}}$  becomes too small to measure and there  
 182 is a significant reduction  $F_{\text{adh}}$  and  $W$  even at the smallest particle concentration used (0.02

183 wt%) where there is no full coverage of nanoparticles. This is consistent with the stable  
184 water film observed using confocal RICM (Fig. 5a). The greatest reductions in  $F_{\text{adh}} = 0.5 \pm$   
185  $0.3$  nN and  $W = 0.8 \pm 0.4 \times 10^{-16}$  J are obtained with 0.1 wt% particle concentrations (by  
186 more than 400 and 7000 times, respectively). However, the differences in  $F_{\text{adh}}$  and  $W$  are  
187 not significant as we vary the particle concentrations from 0.02–0.5 wt%. Since adsorption of  
188 nanoparticles is a random process, there will be spatial variations in resulting micro-/nano-  
189 structures. The exact  $F_{\text{adh}}$  and  $W$  values will therefore depend on where the droplet lands  
190 on the surface. The errors reported for  $F_{\text{adh}}$  in Table 1 are not instrument errors, but rather  
191 reflect the spatial differences micro-/nano-structures. Similar reductions in  $F_{\text{adh}}$  and  $W$  were  
192 also observed as we vary the pH of the nanofluids from 2 to 5 (See Supplemental Figures 1  
193 and 2).

194 We can estimate the contact radius of the droplet  $r$  by noting that  $F = (2\gamma/R)\pi r^2$ ,  
195 where  $\gamma = 50$  mN m<sup>-1</sup> is the water-oil interfacial tension as measured using the pendant  
196 drop’s method and  $2\gamma/R$  is the Laplace pressure inside the microdroplet. At the maximum  
197 loading  $F = 10$  nN,  $r \approx 0.5$   $\mu\text{m}$  which is much larger than the size of the nanoparticles  
198 and similar in size to the spacing between nanoparticles aggregates. The droplet is therefore  
199 in contact with multiple nanoparticles and nanoparticle aggregates. This is in contrast to  
200 chemical force microscopy which uses a sharp nanometric sized solid tip to contact one or at  
201 most a handful of nanoparticles.

202 The nanoparticles and nanoparticle aggregates act as pinning points and droplet probe  
203 AFM can resolve the pinning-depinning dynamics as the droplet detaches from the surface.<sup>29</sup>  
204 In Figures 6d–f, we observe discontinuities in the retract curve with discrete force jumps  $\delta F$   
205  $= 0.1$ – $1$  nN, which correspond to detachment from individual contact points. In contrast,  
206 the retract curve is smooth and continuous in the absence of nanoparticles, since the glass  
207 substrate is homogeneous (in the nanometre scale).

Table 1: Summary of the adhesion force and energy required to detach the oil microdroplet as measured using droplet probe AFM for different nanoparticle (NP) concentrations (See Fig. 6c–f). The errors reported are the standard deviation for at least ten different spots.

| NP conc. (wt%) | $F_{\text{adh}}$ (nN) | $W$ ( $10^{-16}$ J) |
|----------------|-----------------------|---------------------|
| 0              | $210 \pm 10$          | $6000 \pm 1000$     |
| 0.02           | $2.1 \pm 0.6$         | $4 \pm 2$           |
| 0.1            | $0.5 \pm 0.3$         | $0.8 \pm 0.4$       |
| 0.5            | $1.5 \pm 0.7$         | $2 \pm 1$           |

## 208 Relevance to enhanced oil recovery application

209 The wettability of reservoirs plays a critical role in enhanced oil recovery. Traditionally, wet-  
 210 tability alteration is achieved through chemical surfactants, but they are usually expensive  
 211 and do not perform well under high salinity conditions.<sup>36–38</sup> Here, we demonstrate how silica  
 212 nanofluids can be used as effective alternative wetting agents even in the presence of salt.

213 So far we have shown wettability alteration on flat glass surfaces, which are different from  
 214 rock surfaces with irregularly-shaped pores and crevices. We found analogous wettability  
 215 alteration by silica nanofluids on a commercially available microfluidic chip or micromodel  
 216 with etched glass channels that resemble a physical rock network. The micromodel has a  
 217 height  $H = 20 \mu\text{m}$  and a typical channel width  $w \sim 100 \mu\text{m}$ . The glass channels are initially  
 218 hydrophobic but can be rendered hydrophilic by silica nanofluids.<sup>39</sup>

219 As described in our previous publications,<sup>40</sup> we first flowed in 0.2 wt% nanoparticle  
 220 dispersion at flow rates of  $5 \mu\text{L min}^{-1}$  for 30 mins to alter wettability of micromodel, before  
 221 flowing in the oil phase (limonene). To distinguish between water and oil, we have added  
 222 two different fluorescent dyes: Rhodamine 6G in the aqueous phase ( $10 \text{ g L}^{-1}$ , excitation and  
 223 emission wavelengths  $\lambda_{\text{ex, em}} = 488, 525 \text{ nm}$ ) and Nile Red in the oil phase ( $5 \text{ g L}^{-1}$ ,  $\lambda_{\text{ex, em}} =$   
 224  $561, 635 \text{ nm}$ ).

225 The resulting wetting states can then be observed under confocal fluorescence microscopy,  
 226 with the aqueous and oil phase fluorescing green and red lights, respectively (Fig. 7). The  
 227 glass grains inside the micromodel appear black because they do not contain any fluorescent  
 228 dyes. In the absence of nanoparticles, while some water remains, the oil phase is directly in

229 contact with the glass grains whose outlines appear red stained by the Nile Red dye (Fig. 7a).  
 230 In contrast, the nanoparticles are able to stabilize a water film around the glass grains with  
 231 no contact with the oil phase, resulting in more effective oil recovery as will be shown below.

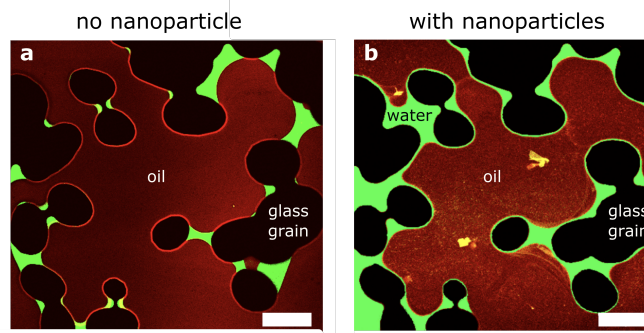


Figure 7: Wetting states of the micromodel (a) without and (b) with nanoparticles. Scale bars are  $100 \mu\text{m}$

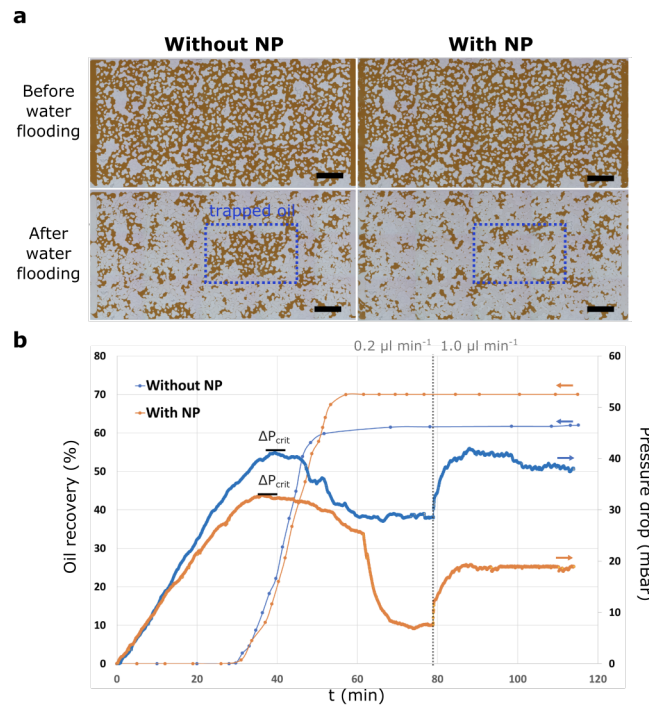


Figure 8: Photographs showing the oil distribution inside microfluidic chips with/without nanoparticle (NP) treatment. Crude oil appears brown, while glass grains and water appear white. Scale bar is 2mm. (b) Oil recovery rates and pressure drop curves during water flooding with and without nanoparticles treatment.

232 To compare the effectiveness of crude oil recovery with and without nanoparticles, we

233 flowed in 3 wt% brine solutions (similar salt content to seawater) at a flow rate of  $0.2 \mu\text{l min}^{-1}$   
234 for 80 minutes before increasing it to  $1.0 \mu\text{l min}^{-1}$ , i.e. water flooding.<sup>41-43</sup> Before water  
235 flooding, the microfluidic channels were filled with crude oil which appear brown (Fig. 8a).  
236 In the absence of nanoparticles, there was a large trapped oil bank in the middle of the  
237 micromodel even after water flooding. With the addition of the nanoparticles, more of the  
238 crude oil was removed including the previously trapped oil bank.

239 We can quantify the oil recovery rates by tracking the area coverage of the crude oil in  
240 the microfluidic chip. After 1 hour of  $0.2 \mu\text{l min}^{-1}$  flow rate, we were able to recover 62% and  
241 70% of the crude oil without and with nanoparticles, respectively, i.e. an improvement of  
242 8% which is significant in EOR applications. There was no further improvement in recovery  
243 rates with longer flow times or increased flow rate of  $1.0 \mu\text{l min}^{-1}$ .

244 We also tracked the pressure drop  $\Delta P$  across the micromodel during the water flooding  
245 process. For oil recovery to happen, the pressure drop must overcome the capillary pressure  
246 and reach a critical pressure  $\Delta P_{\text{crit}} \approx \gamma/(H+w) = 30 \text{ mBar}$ , where  $\gamma = 50 \text{ mN m}^{-1}$  is the oil-  
247 water interfacial tension.<sup>44</sup> The exact  $\Delta P_{\text{crit}}$  depends on the shape of the water-oil meniscus,  
248 in particular the contact angle it makes on the glass grains at the point of displacement.  
249 Experimentally we found that crude oil displacement started at  $t = 30 \text{ min}$ , with  $\Delta P_{\text{crit}} =$   
250  $32 \text{ mBar}$  with nanoparticles lower than  $\Delta P_{\text{crit}} = 42 \text{ mBar}$  without nanoparticles. Beyond  
251 this, the pressure starts to fall and  $\Delta P$  is consistently lower with nanoparticle treatment.

## 252 Conclusions

253 In conclusion, we have demonstrated that fumed silica nanoparticles can form a porous  
254 layer which stabilizes a thin water film, which we can directly visualize using RICM. This  
255 greatly reduces the adhesion of oil droplets even if the surface is only partially covered by  
256 nanoparticles. Using droplet probe AFM, we are able to directly measure the interactions of  
257 an oil microdroplet with the adsorbed nanoparticles, including contact line pinning-depinning

258 dynamics. We also showed how wettability alteration by silica nanoparticles can improve  
259 the oil recovery rate by 8% in a model microfluidic system.

## 260 **Materials and Methods**

261 **Materials and chemicals.** Hydrophilic fumed silica nanoparticles were obtained from  
262 Evonik Industries. They have an average primary particle size of 7 nm and specific sur-  
263 face area of  $300 \text{ m}^2 \text{ g}^{-1}$ . Microscope slides were purchased from AmScope. Limonene was  
264 purchased from Fisher Scientific, while Rhodamine 6G dye, Nile Red dyes, sodium chloride  
265 (NaCl) and silicone oil (Polyphenyl-methylsiloxane with viscosity around 100 mPa.s and  
266 density 1.06 g/ml) were purchased from Sigma-Aldrich. Reprorubber Thin Pour silicone  
267 elastomer (two-part cure) was purchased from Flexbar. All chemicals were used as received.  
268 Deionized (DI) water with a resistivity of  $17 \text{ M}\Omega \text{ cm}$  was used as the aqueous phase. The  
269 crude oil has a density of 0.89 g/ml and viscosity of 41 mPa s.

270 The micromodel was purchased from Micronit Micro Technologies. The pore structure in  
271 the microfluidic chip, based on the structure of a physical rock, is etched with hydrofluoric  
272 acid and the surface is initially hydrophobic. The microfluidic channels have a height  $H =$   
273  $20 \mu\text{m}$  and a permeability of 2.5 Darcy. Pore structure and parameters of the micromodel  
274 can be found in our previous publication.<sup>40</sup>

275 **Preparation of nanofluids.** Three nanoparticle concentrations (0.02, 0.1 and 0.5 wt%)  
276 were dispersed in 3 wt% NaCl aqueous solution (brine) using an ultrasonicator (UP400St,  
277 Hielscher, Germany). The pH of nanofluid was adjusted by adding concentrated hydrochloric  
278 acid (HCl). Note that the pH of DI water is lowered by the addition of nanoparticles which  
279 have a large surface-to-volume ratio ( $300 \text{ m}^2 \text{ g}^{-1}$ ). For example, a 1 wt% nanoparticle  
280 concentration lowers the pH to 4.8 even without HCl.

281 **Wettability alteration of glass surfaces.** Glass substrates (2 cm by 2 cm) were  
282 cut to size from microscope slides and soaked in nanofluid/brine solution for 1 hour. The

283 glass substrates with the adsorbed nanoparticle layer were then rinsed (to remove any loose  
284 nanoparticles) and transferred to a petri-dish of brine water for further experiments, e.g.  
285 droplet probe AFM.

286 **Cryo-SEM imaging.** Prior to cryo-preparation, each sample was immersed in nanoflu-  
287 ids with different concentrations for one hour and then rinsed with deionized water to remove  
288 the salt and free nanoparticles. Next, the samples were cooled by plunging into a nitrogen  
289 slush at atmospheric pressure. Then the samples were frozen at  $-120^{\circ}\text{C}$ , etched for 300 s at  
290  $-95^{\circ}\text{C}$ , and sputtered with gold in the cryo-preparation chamber. After preparation, samples  
291 were transferred into the SEM chamber (JSM-6700F, JEOL, Japan) for imaging.

292 **AFM topography measurements.** Before exposing the glass surface to the nanofluid,  
293 a portion of the surface was covered with Reprorubber silicone elastomer. After soaking the  
294 surface in nanofluid for about an hour, the silicone elastomer was peeled off to reveal the  
295 underlying glass substrate. AFM topography (JPK Instrument) was performed under water  
296 at the boundary between the bare glass surface (previously covered by elastomer) and the  
297 nanoparticle layer.

298 **Confocal RICM.** We first deposited a millimetric-sized oil droplet on the substrate  
299 of interest under water. RICM was performed using a confocal laser scanning microscope  
300 (FV3000RS; Olympus Corporation). During the experiment we raster scanned the surface  
301 with one focused beam of monochromatic light with wavelength  $\gamma=561$  nm, and captured the  
302 reflected light through the pinhole of a confocal microscope; thus, only reflected light from  
303 the focal plane, that was, the interface of interest, was able to reach the photomultiplier  
304 tube of the microscope.<sup>26</sup> In the presence of a thin water film, the light reflected off the  
305 solid/water and water/oil droplet interfaces would interfere with one another constructively  
306 or destructively to give bright or dark fringes, respectively.

307 **Droplet probe AFM.** To create small oil droplets, we force  $60\ \mu\text{l}$  of oil through a  
308 small capillary tube with inner and outer diameters of  $360\ \mu\text{m}$  and  $290\ \mu\text{m}$  into a petri-dish  
309 of water. This generates multiple droplets with a broad range of sizes  $2R = 20\text{--}200\ \mu\text{m}$ .

310 We can then pick up a droplet of the desired size (approximately  $20 \mu\text{m}$ ) using a tipless  
311 silicon cantilever, with dimensions width  $w = 50 \mu\text{m}$  and length  $l = 450 \mu\text{m}$ , and a spring  
312 constant  $k = 0.2 \text{ N m}^{-1}$  as determined using Sader’s method. Once picked up, the droplet  
313 adheres much more strongly to cantilever than to the surface, allowing us to perform force  
314 spectroscopy measurements on the surface of interest multiple times without detaching. For  
315 each surface, we performed force spectroscopy measurements for at least 10 different spots,  
316 with 3–5 repeats on each spot. During each force spectroscopy measurement, the droplet  
317 approaches and retracts from the surface at a controlled speed  $U = 2 \mu\text{m s}^{-1}$ , with the force  
318 experienced by the droplet inferred from the cantilever deflection  $\delta_z$ , since  $F = k \delta_z$ .  $\delta_z$  is  
319 detected by shining a laser light (infrared, wavelength of 980 nm) onto the cantilever, which  
320 is reflected into a 4-quadrant sensor. More details can be found in our previous publication.<sup>29</sup>

321 **Microfluidic flooding experiment.** The micromodels were first completely filled with  
322 3 wt% NaCl brine solution. To alter the wettability of the micromodel, we injected 1 wt%  
323 silica nanofluids for 1 hour at  $1 \mu\text{l min}^{-1}$  flow rate; for the control, no nanofluid was injected.  
324 The crude oil was then injected at  $1 \mu\text{l min}^{-1}$  flow rate for 1 hour. To recover the crude  
325 oil, 3 wt% NaCl brine solution was again injected first at  $0.2 \mu\text{l min}^{-1}$  flow rate for 80 min,  
326 before increasing it to  $1.0 \mu\text{l min}^{-1}$

327 Local images of the micromodel were taken using Leica digital microscope DVM6 and  
328 then stitched to get a whole picture of the micromodel. ImageJ was used to perform image  
329 analysis for oil recovery calculations. Pressure drop across the micromodel was recorded  
330 during water flooding.

## 331 Acknowledgement

332 This research was supported by the Agency for Science, Technology and Research (A\*STAR),  
333 Singapore, under IAFPP Programme (project title: Advanced Functional Polymer Particle  
334 Technologies for the Oil and Gas Industry; grant no.: A18B4a0094) as well as the Petroleum

335 Engineering Professorship Grant from the Economic Development Board of Singapore. The  
336 authors would like to thank Ms. Jing Lin Inez Kwek for her help with Cryo-SEM imaging.

## 337 **Supporting Information Available**

338 Additional experimental data can be found in the Supporting Information.

## 339 **References**

- 340 (1) Taylor, R.; Coulombe, S.; Otanicar, T.; Phelan, P.; Gunawan, A.; Lv, W.; Rosen-  
341 garten, G.; Prasher, R.; Tyagi, H. Small Particles, Big Impacts: A Review of the  
342 Diverse Applications of Nanofluids. *J. Appl. Phys.* **2013**, *113*, 1.
- 343 (2) Eltoum, H.; Yang, Y.-.; Hou, J.-R. The Effect of Nanoparticles on Reservoir Wettability  
344 Alteration: a Critical Review. *Petroleum Sci.* **2020**, 1–18.
- 345 (3) Wasan, D. T.; Nikolov, A. D. Spreading of Nanofluids on Solids. *Nature* **2003**, *423*,  
346 156–159.
- 347 (4) Coursey, J. S.; Kim, J. Nanofluid Boiling: The Effect of Surface Wettability. *Int. J.*  
348 *Heat Fluid Fl.* **2008**, *29*, 1577–1585.
- 349 (5) Kong, X.; Ohadi, M. M. Applications of Micro and Nano Technologies in the Oil and  
350 Gas Industry-Overview of the Recent Progress. Abu Dhabi International Petroleum  
351 Exhibition and Conference. 2010.
- 352 (6) Lau, H. C.; Yu, M.; Nguyen, Q. P. Nanotechnology for Oilfield Applications: Challenges  
353 and Impact. *J. Petrol. Sci. Eng.* **2017**, *157*, 1160–1169.
- 354 (7) Li, S.; Hendraningrat, L.; Torsaeter, O. Improved Oil Recovery by Hydrophilic Silica  
355 Nanoparticles Suspension: 2 Phase Flow Experimental Studies. IPTC 2013: Interna-  
356 tional Petroleum Technology Conference. 2013; p 350.

- 357 (8) Moghaddam, R. N.; Bahramian, A.; Fakhroueian, Z.; Karimi, A.; Arya, S. Comparative  
358 Study of using Nanoparticles for Enhanced Oil Recovery: Wettability Alteration of  
359 Carbonate Rocks. *Energy Fuels* **2015**, *29*, 2111–2119.
- 360 (9) Dehghan Monfared, A.; Ghazanfari, M. H.; Jamialahmadi, M.; Helalizadeh, A. Poten-  
361 tial Application of Silica Nanoparticles for Wettability Alteration of Oil–Wet Calcite:  
362 a Mechanistic Study. *Energy & Fuels* **2016**, *30*, 3947–3961.
- 363 (10) Ni, X.; Jiang, G.; Liu, F.; Deng, Z. Synthesis of an Amphiphobic Nanofluid with a Novel  
364 Structure and its Wettability Alteration on Low-permeability Sandstone Reservoirs.  
365 *Energy Fuels* **2018**, *32*, 4747–4753.
- 366 (11) Afekare, D.; Garno, J.; Rao, D. Enhancing Oil Recovery using Silica Nanoparticles:  
367 Nanoscale Wettability Alteration Effects and Implications for Shale Oil Recovery. *J.*  
368 *Pet. Sci. Eng.* **2021**, *203*, 108897.
- 369 (12) Lim, S.; Horiuchi, H.; Nikolov, A. D.; Wasan, D. Nanofluids Alter the Surface Wettability  
370 of Solids. *Langmuir* **2015**, *31*, 5827–5835.
- 371 (13) Andrew, M.; Bijeljic, B.; Blunt, M. J. Pore-Scale Contact Angle Measurements at  
372 Reservoir Conditions using X-ray Microtomography. *Adv. Water Resour.* **2014**, *68*,  
373 24–31.
- 374 (14) Mirchi, V. Pore-Scale Investigation of the Effect of Surfactant on Fluid Occupancies  
375 during Low-Salinity Waterflooding in Oil-Wet Carbonates. SPE Annual Technical Con-  
376 ference and Exhibition. 2018.
- 377 (15) Decker, E. L.; Frank, B.; Suo, Y.; Garoff, S. Physics of Contact Angle Measurement.  
378 *Colloids Surf. A Physicochem. Eng. Asp.* **1999**, *156*, 177–189.
- 379 (16) Schellenberger, F.; Encinas, N.; Vollmer, D.; Butt, H.-J. How Water Advances on  
380 Superhydrophobic Surfaces. *Phys. Rev. Lett.* **2016**, *116*, 096101.

- 381 (17) Liu, K.; Vuckovac, M.; Latikka, M.; Huhtamäki, T.; Ras, R. H. A. Improving Surface-  
382 Wetting Characterization. *Science* **2019**, *363*, 1147–1148.
- 383 (18) Srinivasan, S.; McKinley, G. H.; Cohen, R. E. Assessing the Accuracy of Contact Angle  
384 Measurements for Sessile Drops on Liquid-Repellent Surfaces. *Langmuir* **2011**, *27*,  
385 13582–13589.
- 386 (19) Javadpour, F.; Farshi, M. M.; Amrein, M. Atomic-Force Microscopy: a New Tool for  
387 Gas-Shale Characterization. *J. Can. Pet. Technol.* **2012**, *51*, 236–243.
- 388 (20) Yang, J.; Hatcherian, J.; Hackley, P. C.; Pomerantz, A. E. Nanoscale Geochemical and  
389 Geomechanical Characterization of Organic Matter in Shale. *Nat. Comm.* **2017**, *8*, 1–9.
- 390 (21) Hilner, E.; Andersson, M. P.; Hassenkam, T.; Matthiesen, J.; Salino, P.; Stipp, S. L. S.  
391 The Effect of Ionic Strength on Oil Adhesion in Sandstone—the Search for the Low  
392 Salinity Mechanism. *Sci. Rep.* **2015**, *5*, 1–9.
- 393 (22) Afekare, D. Enhancing Oil Recovery Using Aqueous Dispersions of Silicon Dioxide  
394 Nanoparticles: The Search for Nanoscale Wettability Alteration Mechanism. SPE An-  
395 nual Technical Conference and Exhibition. 2020.
- 396 (23) Afekare, D.; Garno, J. C.; Rao, D. Insights into Nanoscale Wettability Effects of Low  
397 Salinity and Nanofluid Enhanced Oil Recovery Techniques. *Energies* **2020**, *13*, 4443.
- 398 (24) Hendraningrat, L.; Li, S.; Torsæter, O. A Coreflood Investigation of Nanofluid En-  
399 hanced Oil Recovery. *J. Pet. Sci. Eng.* **2013**, *111*, 128–138.
- 400 (25) Limozin, L.; Sengupta, K. Quantitative Reflection Interference Contrast Microscopy  
401 (RICM) in Soft Matter and Cell Adhesion. *ChemPhysChem* **2009**, *10*, 2752–2768.
- 402 (26) Daniel, D.; Timonen, J. V. I.; Li, R.; Velling, S. J.; Aizenberg, J. Oleoplaning Droplets  
403 on Lubricated Surfaces. *Nat. Phys.* **2017**, *13*, 1020.

- 404 (27) Quéré, D. Wetting and Roughness. *Annu. Rev. Mater. Res.* **2008**, *38*, 71–99.
- 405 (28) Liu, M.; Wang, S.; Wei, Z.; Song, Y.; Jiang, L. Bioinspired Design of a Superoleophobic  
406 and Low Adhesive Water/Solid Interface. *Adv. Mater.* **2009**, *21*, 665–669.
- 407 (29) Daniel, D.; Lay, C. L.; Sng, A.; Lee, C. J. J.; Neo, D. C. J.; Ling, X. Y.; Tomczak, N.  
408 Mapping Micrometer-Scale Wetting Properties of Superhydrophobic Surfaces. *Proc.*  
409 *Natl. Acad. Sci. U.S.A.* **2019**, *116*, 25008–25012.
- 410 (30) Daniel, D.; Florida, Y.; Lay, C. L.; Koh, X. Q.; Sng, A.; Tomczak, N. Quantifying  
411 Surface Wetting Properties Using Droplet Probe Atomic Force Microscopy. *ACS Appl.*  
412 *Mater. Interfaces* **2020**, *12*, 42386–42392.
- 413 (31) Xie, L.; Shi, C.; Cui, X.; Zeng, H. Surface Forces and Interaction Mechanisms of Emul-  
414 sion Drops and Gas Bubbles in Complex Fluids. *Langmuir* **2017**, *33*, 3911–3925.
- 415 (32) Israelachvili, J. N. *Intermolecular and Surface Forces*; Academic press, 2011; Chapter  
416 14.
- 417 (33) Lin, M. Y.; Lindsay, H. M.; Weitz, D. A.; Ball, R. C.; Klein, R.; Meakin, P. Universality  
418 in Colloid Aggregation. *Nature* **1989**, *339*, 360–362.
- 419 (34) Born, M.; Wolf, E. *Principles of Optics: Electromagnetic Theory of Propagation, In-*  
420 *terference and Diffraction of Light*; Elsevier, 2013.
- 421 (35) Butt, H.-J.; Cappella, B.; Kappl, M. Force Measurements with the Atomic Force Mi-  
422 croscope: Technique, Interpretation and Applications. *Surf. Sci. Rep.* **2005**, *59*, 1–152.
- 423 (36) Al-Ansari, S.; Arif, M.; Wang, S.; Barifcani, A.; Lebedev, M.; Iglauer, S. Wettability  
424 of nanofluid-modified oil-wet calcite at reservoir conditions. *Fuel* **2018**, *211*, 405–414.
- 425 (37) Liu, F.; Wang, M. Review of Low Salinity Waterflooding Mechanisms: Wettability  
426 Alteration and its Impact on Oil Recovery. *Fuel* **2020**, *267*, 117112.

- 427 (38) bin Dahbag, M.; Al-Gawfi, A.; Hassanzadeh, H. Suitability of Hot Urea Solutions for  
428 Wettability Alteration of Bitumen Reservoirs–Simulation of Laboratory Flooding Ex-  
429 periments. *Fuel* **2020**, *272*, 117713.
- 430 (39) Ramakrishnaiah, R.; Alkheraif, A. A.; Divakar, D. D.; Matinlinna, J. P.; Vallittu, P. K.  
431 The Effect of Hydrofluoric Acid Etching Duration on the Surface Micromorphology,  
432 Roughness, and Wettability of Dental Ceramics. *Int. J. Mol. Sci* **2016**, *17*, 822.
- 433 (40) Li, S.; Daniel, D.; Lau, H. C.; Hadia, N. J.; Torsæter, O.; Stubbs, L. P. Investigation  
434 of Wettability Alteration by Silica Nanoparticles Through Advanced Surface-Wetting  
435 Visualization Techniques. SPE Annual Technical Conference and Exhibition. 2019.
- 436 (41) Li, S.; Torsæter, O.; Lau, H. C.; Hadia, N. J.; Stubbs, L. P. The Impact of Nanoparticle  
437 Adsorption on Transport and Wettability Alteration in Water-Wet Berea Sandstone:  
438 An Experimental Study. *Front. Phys.* **2019**, *7*, 74.
- 439 (42) Li, S.; Hadia, N. J.; Lau, H. C.; Torsæter, O.; Stubbs, L. P.; Ng, Q. H. Silica Nanoparti-  
440 cles Suspension for Enhanced Oil Recovery: Stability Behavior and Flow Visualization.  
441 80th EAGE Conference and Exhibition. 2018.
- 442 (43) Li, S.; Genys, M.; Wang, K.; Torsæter, O. Experimental Study of Wettability Alteration  
443 During Nanofluid Enhanced Oil Recovery Process and its Effect on Oil Recovery. SPE  
444 Reservoir Characterisation and Simulation Conference and Exhibition. 2015.
- 445 (44) de Gennes, P.-G.; Brochard-Wyart, F.; Quéré, D. *Capillarity and Wetting Phenomena:*  
446 *Drops, Bubbles, Pearls, Waves*; Springer, 2004.

447 **Graphical TOC Entry**

448

